IET Optoelectronics

Special Issue: Selected Papers from Semiconductor and Integrated Optoelectronics (SIOE) 2019

IET Journals
The Institution of Engineering and Technology

Design conditions in the middle range for implementation of integrated ring resonators in $LiNbO_3$ by direct laser writing

ISSN 1751-8768
Received on 25th June 2019
Revised 17th October 2019
Accepted on 4th December 2019
E-First on 4th February 2020
doi: 10.1049/iet-opt.2019.0068
www.ietdl.org

Paula L. Pagano[1,2,3], Damián Presti[1,4], Roberto R. Peyton[1,4], Fabian A. Videla[1,5], Gustavo A. Torchia[1,4] ✉

[1]*Centro de Investigaciones Ópticas (CONICET-CICBA-UNLP), M.B. Gonnet (1897), Buenos Aires, Argentina*
[2]*Departamento de Física, Facultad de Ciencias Exactas, Universidad Nacional de La Plata, Calle 115 y 47, Argentina*
[3]*Consejo Interuniversitario Nacional, Argentina*
[4]*Departamento De Ciencia y Tecnología, Universidad Nacional de Quilmes, Roque Sáenz Peña 352 – Bernal (1876) – Bs. As., Argentina*
[5]*Departamento de Ciencias Básicas, Facultad de Ingeniería, Universidad Nacional de la Plata, Calle 115 y 47, Argentina*
✉ *E-mail: gustavot@ciop.unlp.edu.ar*

Abstract: The aim of this work is to design an integrated optical ring resonator to be implemented in $LiNbO_3$ with a 2.5 mm radius and an operating wavelength of 1550 nm. Considering these ring parameters, a free spectral range of 71.54 pm and a quality factor of $\sim 5 \times 10^5$ were calculated. The authors apply results to improve the implementation of femtosecond laser writing in lithium niobate crystals. As it is well-known finite difference time domain method requires large memory and time for processing circuits with large footprint (few square mm), in contrast, the beam propagation method allows to simulate large bends in a simple way. RSoft suite design tools commonly represent circles by closed polygons whose geometrical parameters are not optimised to obtain bending losses as least as possible, as suggested by coherent coupling theory. In this sense, the suitable determination of a splice angle (in this case $1.44°$), shape and length for segments are key parameters in the ring design. For this purpose, an *ad hoc* software was implemented to overcome this drawback. In summary, a 250 sided polygon side showed a suitable coupling performance and established a new layout approach for middle range rings.

1 Introduction

A ring resonator is yet another implementation of the Sagnac effect and was first implemented as a fibre optic gyroscope. This type of gyroscope uses a recirculating wave to enhance the phase differences induced by the Sagnac effect (counterclockwise and clockwise propagation) when the sensor is rotated. The light enters and leaves the ring cavity through a coupler into the detector. In contrast, for an integrated ring resonator the principle of operation is based on a ring cavity operating like a Fabry-Perot interferometer, with multiple interference between the recirculating waves. Resonance can be achieved by sweeping the frequency of the light or by modifying the optical length in the ring, thus resulting in a constructive interference being maximum the light intensity trapped in the resonator [1, 2].

When relatively large rings are implemented for simulations it is necessary to study how to overpass certain software constraints. Simulation softwares are normally based on finite differential time domain (FDTD) or beam propagation method (BPM). Use of these mathematical methods for integrated optical circuits and implementation techniques is indeed challenging, because the size of rings determine the algorithm selected. To clarify the criteria of selection between both algorithms, we discuss the following arguments: FDTD allows back-propagation, but BPM-based software does not. However, it enables to simulate larger rings than FDTD ($r < 200\ \mu$m) if a specific strategy is performed as we introduce in this paper. Additionally, FDTD is memory and time consuming. Layout tools belonging to the software is a relevant aspect because define the polygonal geometries that replace, in fact, the exact circular geometry. Of course, the refractive index profile of the selected material plays an important role, so below we describe its features.

Lithium niobate ($LiNbO_3$) is a renowned ferroelectric crystal used for electro-optic and non-linear optical applications. Its large acoustooptic and piezoelectric coefficients make it an ideal material also for optoelectronics and sensor applications [3]. For example, on the receiver side micro-ring resonators can be used as high-speed filters for single wavelength channels being received from the network. The electro-optic effect of the proposed material enables the fast switching on–off of the resonating wavelength [3]. In this sense, a new generation of high integrated devices can be found in [4].

A high quality factor in a $LiNbO_3$ integrated optical circular ring resonator designed for optical angular rate sensing was reported in [5–7]. Likewise, Johnson and Leonberger [8] report very-low-loss Ti:$LiNbO_3$ coherently coupled waveguide bend structures. The losses through successive coupled bends are found to be substantially less than the losses through comparable numbers of otherwise identical isolated bends.

Similar ring resonators designed as polygons had been studied by other authors who consider its featuring parameters like quality factor, free spectral range (FSR), contrast ratio and so on [9]. However, these papers did not emphasise how the software tools work in detail, influencing the final design. Bending losses being a critical parameter related with the higher quality factor goal, it was important to determine a suitable geometry based on a regular polygon in order to minimise them. In this sense, we formulate a design criterion based on simulation results. The correct number of sides (each side is really a track representing a waveguide), the splice angle and the appropriate refractive index profile are the main items to choose, in this formulation.

Losses by scattering vary in a sensitive form when the amplitude peaks of the index profile curves are changed. An increase in the amplitude corresponds to a meaningful reduction in the observed scattering. Another interesting parameter is the splice angle in order to minimise bending losses, which is related with the coherent coupling theory. In turn, the reduction in the number of sides was analysed considering each corner as a source of dispersion. Functionally described, losses depend on the length of each segment in an oscillatory form, see e.g. [10] in agreement with the coherent coupling theory. We show that scattering losses were reduced by designing the track geometry with a trapezoidal shape, improving the coupling behaviour in the splices.

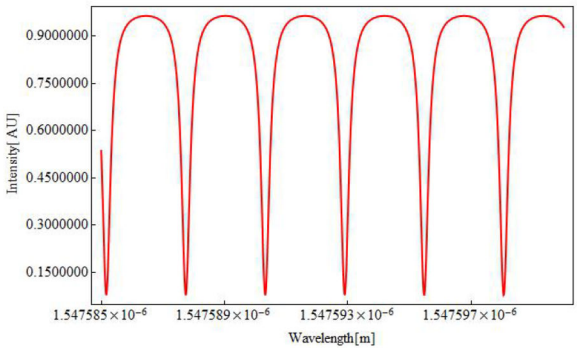

Fig. 1 *Transfer function obtained for a ring with 2.5 mm radius at 1550 nm wavelength*

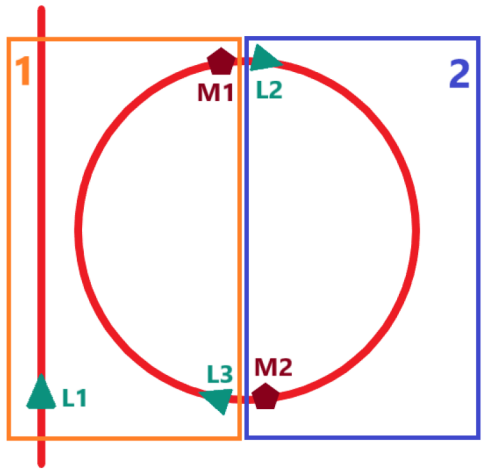

Fig. 2 *Scheme of simulation zones. The light blue triangles show the position of the launcher ((L1 and L3) from zone 1. L2 is the launcher for zone 2. The dark red pentagon (M1 and M2) indicates the monitor position*

Some integrated prototypes successfully demonstrated that by low loss technology, design of high-Q ($\geq 10^6$) resonator is possible [11, 12].

In summary, in order to minimise bending losses for $LiNbO_3$ ring resonators implemented by direct laser writing, we present several strategies to simulate large ring resonators by means of BPM software which provides suitable results for designing these kinds of optical devices (Table 1).

2 Ring resonator features

We present some typical characteristics from the device to compare its performance against others. For this purpose, we calculate its transfer function. Ring resonators can be featured by some typical parameters like the FSR, finesse, resolution, electro-optical response, all of them summarised in the transfer function [3, 6, 13] whose expression is

$$T(\lambda) = \frac{t^2 + e^{-2\pi\alpha r} - 2e^{-\alpha\pi r}t\cos(2\pi n_{\text{eff}}(2\pi r/\lambda))}{1 + e^{-2\pi\alpha r}t^2 - 2te^{-\alpha\pi r}\cos(2\pi n_{\text{eff}}(2\pi r/\lambda))} \quad (1)$$

where n_{eff} is the effective refractive index whose value is 2.2137, α is the attenuation estimated in 0.41 m^{-1}, r is the ring radius and t is the transmittance whose value is 0.866. This value was obtained through the expression $t = \sqrt{1-\kappa^2}$ where κ the coupling coefficient is 0.5 assuming a ring with around 7 dB of losses as was reported in [14, 15]. Both effective refractive index and attenuation were obtained from R-Soft software handbook. Fig. 1 shows the transfer function obtained using the previous expression. Then, in Table 2 we showed the parameters for the ring we proposed. As it is expected, a diminishing quality factor by 50% and a FSR increasing from 3 to 70 pm were observed for our ring in comparison with a fibre ring resonators (radius ~10 cm) [16].

Table 1 Typical parameters for a ring resonator and our calculated values

Ring parameters	Values
FSR	68.84 pm
FWHM	3.22 pm
finesse	21.40
quality factor	4.81×10^5
radius	2.5 mm
attenuation (α)	$4.15 \times 10^{-1}\ m^{-1}$
loss	0.997
transmittance	0.866

Table 2 Coefficients values of (2)

Coefficients	Values
a	0.083
a_t	60
b_t	20 μm^{-2}
w	0.075 μm^{-2}
c_1	0.012 μm^{-2}
c_2	0.0125 μm^{-2}
d	18 μm
gap_w	14.286 μm

Finesse and full wave at half maximum (FWHM) vary in consequence.

Although the mathematical model corresponds to a circular ring, results obtained well represents the characteristic behaviour of our polygonal ring design.

3 Methods

As a simulation strategy to run the BPM algorithm, the ring was piecewise simulated as it is sketched in Fig. 2.

In agreement with Fig. 2, simulations of propagated light were made in two regions, the first one (zone 1) includes the straight or 'bus' waveguide and the left side of the ring. Coupling takes place in this region. In order to measure the cross-coupled energy, on the bottom and the top of this zone, the L1 launcher and M1 monitor were added, respectively. The second one includes the right side of the ring (zone 2) where no coupling takes place. We locate a source of light L2 in the upper part of the figure while in the lower part, monitor M2 (dark red pentagon) was included.

To make the desired geometry, the donnut (torus) tool was used to implement the ring resonator scheme. This structure physically corresponds to a waveguide, so a refractive index must be associated with it. The index profile assigned takes values that faithfully represent changes obtained after a femtosecond laser writing process [17].

Through femtosecond laser technique, direct writing will induce negative refractive-index changes in the directly irradiated region, causing expansion of the lattices in the focal volume. This dilation of the local region (i.e. in the track core) is generally associated with refractive-index reduction ($\Delta n \sim -10^{-3}$), and the neighbourhood regions possess a relatively high index ($\Delta n \sim (2-4) \times 10^{-3}$) through the stress-induced effects [18]. These waveguides show low propagation losses and allow implementing electro-optic modulators; using the quasi-phase matching technique, these waveguides can be used as well as to perform efficient second harmonic generation and optical parametric generation/amplification [3].

The well-accepted configuration classification depends on the induced refractive-index changes in the laser-irradiated regions. So, for typical waveguides in dielectric crystals the literature defines, Type I (index increased in the irradiated region) and Type II (index decreased in the irradiated regions, typically in the form of damage tracks). Usually, if there are two parallel tracks (with lengths of 15–30 μm or more) with suitable separation (typically 10–20 μm), the

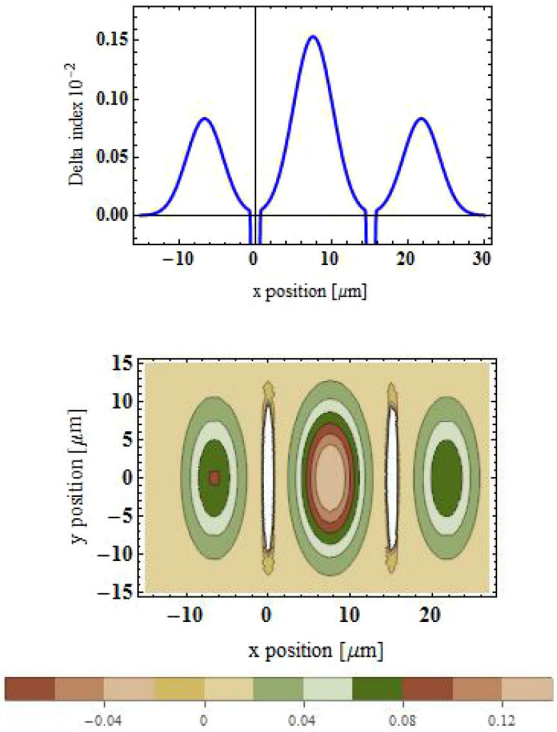

Fig. 3 *Index profile distribution and front view of section A-A'(see Fig. 5a). Whole double track. In white, the two barrier zones, featured by its high negative refractive index variation*

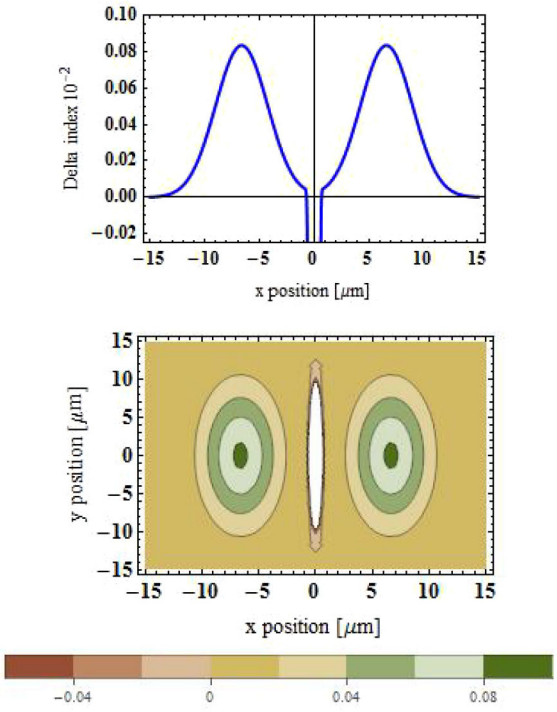

Fig. 4 *Index profile distribution and front view of sections B-B′ and C-C′ (see Fig. 5a). One side of a double track*

waveguide core is therefore located in the region between the two tracks, i.e. the so-called 'double-line' or 'dual line' approach. Dual-line geometry is the Type II most preferred design for build crystals waveguides [18].

The refractive index profile distribution described can be better appreciated through Figs. 3 and 4. The function that describes the cross-section of the index is given by the following expression [19]:

$$\begin{aligned} f(x,y) = {} & e^{-c_1(d+e.x)^2} + ae^{-c_2y^2}e^{-c_1y^2}e^{-c_1(-d+e.x)^2} \\ & -a_te^{-b_tx^2}e^{-c_2y^2} - a_te^{-b_t(x+gap_w)^2}e^{-wy^2} \\ & +ae^{-c_2y^2}e^{-c_1[-d+e(x+gap_w)^2]} + e^{-c_1[d+e(x-gap_w)]^2} \end{aligned} \quad (2)$$

Coefficients of (2) are summarised in Table 2.

As it can be seen, the expression is basically a Gaussian sum, where its main parameters are central position, width and amplitude (positives and negatives). In this form, the refractive index profile can be reproduced with enough accuracy to simulate the real behaviour. The guiding performance of tracks highly depend on this function and is interesting to observe how changes in the different coefficient modify the confined power. It must be mentioned that, each of them is related to physical parameters of the writing laser such as fluency, focusing and intensity of the beam [20].

As we show in Fig. 5, we used different index profiles. This is because the software does not interpret two profiles overlapped as a sum. To overcome this drawback, a profile corresponding to the sum was inserted when single Gaussian profiles result superimposed (Fig. 3). In other sectors separation between maxima of Gaussians were greater, other index profiles were used as can be appreciated in Fig. 4.

4 Results and discussion

4.1 Designing

The donnut tool (R-Soft) really draws a polygon, defined with a splice angle slightly larger than the convenient value to reduce the losses associated with bends. Due to the coherent coupling effect, the transmission of these two bending waveguides are almost the same for $\theta \leq 0°$. When $\theta > 0°$, the bend angle is so large that radiation mode cannot be completely coupled back to the waveguide, and therefore, the normalised transmitted power is greatly decreased [21]. Some design techniques at low splice angles are considered in [22]. However, simulation shows that for ring design the constrain over the spice angle of 0.9° can be relaxed to 1.44° reducing the amount of segments. Then, we designed a 250 sided polygon using an *ad-hoc* program. The energy initially transferred to unguided modes can be returned to the guided mode, resulting in a minimum of the loss curves proposed by Taylor [10] for circular bends. For our design this value correspond to 1.3 obtained from $(n_g - n_b)L/\lambda$, (the ordinate of the curve in that publication), here n_g is the maximum refractive index of the guide, n_b is the lower refractive index value. The delta index negative region is well known as 'barrier' to express its confinement property. L is the length of the polygon side, partially represented in Fig. 6. Individual polygons (parallelograms in the insert of Fig. 6) present in the minor side an appreciable slope referred to the horizontal. This detailed design allows us to achieve lower splice angles between tracks, and consequently, bending losses can be reduced. Conversely, R-Soft does not allow this geometric possibility with tool for drawing segments. Once defined the geometry, the proposed index profile was assigned to each side (track). As a result, the contour map of Fig. 5 was constructed. For the sake of clarity, we present a brief description of Fig. 5. Each black line represents a track written directly by the laser spot. In a double track design, below to the writing zone, the refractive index decreases, being a negative change referred to as the initial value. In contrast, between the black lines (strong mechanically stressed regions), it can be seen that red lines represent zones with the highest refractive indexes (positive changes of refractive indexes) where light must be mainly confined. The blue lines have a positive change in the refractive index, but its values are lower than in red regions. The previously proposed changes in the refractive index, given by the Gaussian of the resultant profile, concentrate the variation closest to the red region represented in Fig. 5.

4.2 Simulated ring performance

First, our simulation procedure starts in zone 1 illuminated by the L1 launcher. Through the monitor (M1), the amplitude and phase

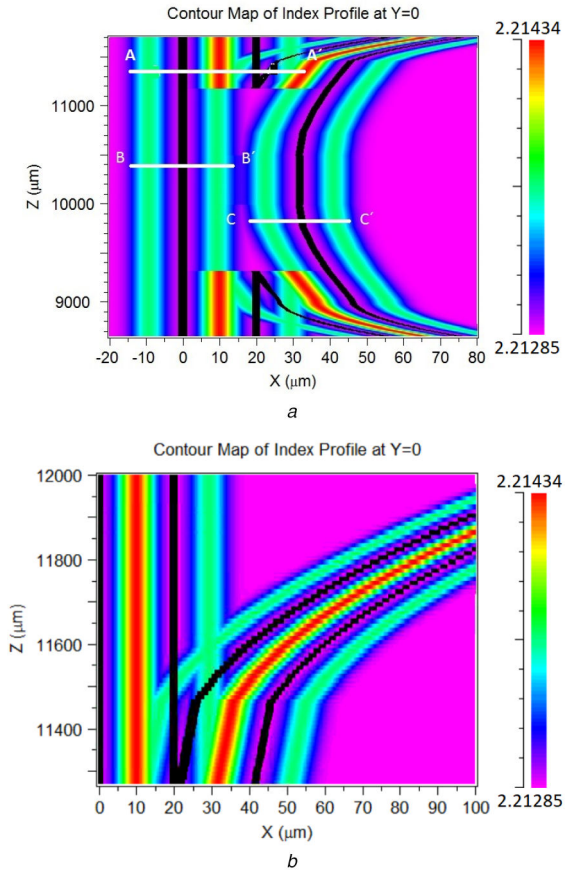

Fig. 5 *Contour map of index profile at y = 0*
(a) Left side of the ring, ***(b)*** Zoom of the upper sector, this shows the different polygon edges

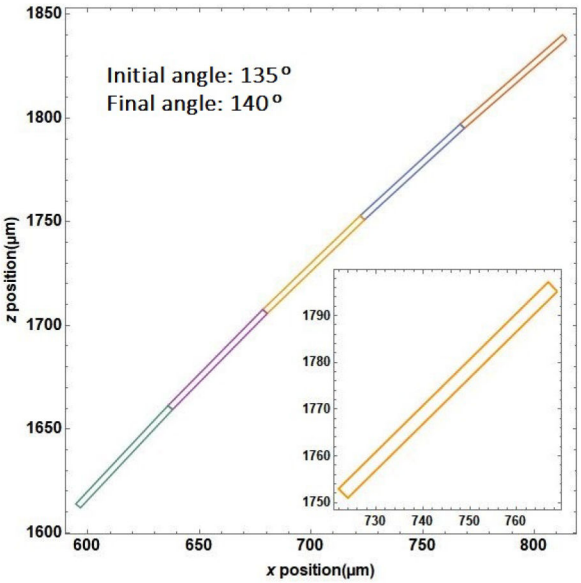

Fig. 6 *Arc segment traced by an ad-hoc program*

of the field at the upper part of zone 1 were stored. We assumed negligible the losses in zone 2. Due to this, calculated values were re-injected to the launcher L3, so, in this way, we simulated one round of the light in the ring (Figs. 7 and 8). Each mentioned zone corresponds to different profiles of refractive index got by a combination of the refractive indexes presented in Figs. 3 and 4. Those profiles were introduced as refractive index distribution in R-soft (Fig. 5).

When zone 1 (a combination between the bus and the left part of the ring) is simulated, coupling in the upper part of the ring can be appreciated. This shows the suitable dimensions of the 'gap'

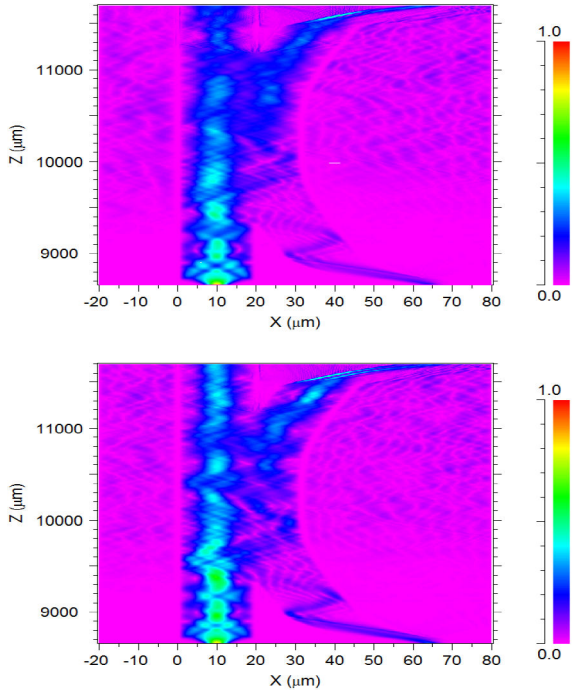

Fig. 7 *Simulations of one round of the light in the ring obtained before multiplied 'a' by 2 and 3 (respectively)*

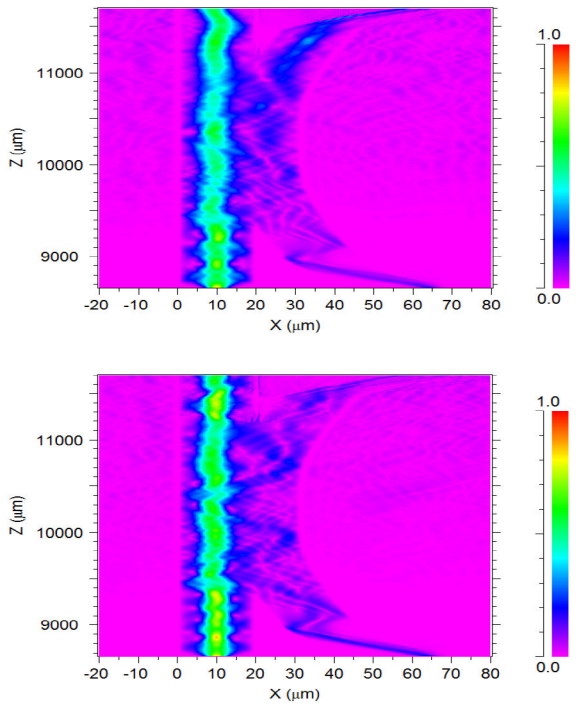

Fig. 8 *Simulations of one round of the light in the ring obtained before multiplied 'a' by 5 and 8 (respectively)*

(distance between the bus and the ring) allowing energy transfer. The lower part of the ring shows similar intensities through them, as seen in the colour map shown (see Figs. 7–9). The region corresponding to the bus waveguide shows changes of intensity near the gap where a decreasing can be observed because of energy derived to the ring. In this form, we verify the correct selection of the splice angle and the length of the side. However, some scattering could be observed. To reduce this effect, we first tried different grid resolutions. However, no positive results were obtained.

Considering that light confinement depends on index contrast between waveguide and substrate, we changed the amplitude of the Gaussian index profile curve, modifying the '*a*' coefficient of expression (2).

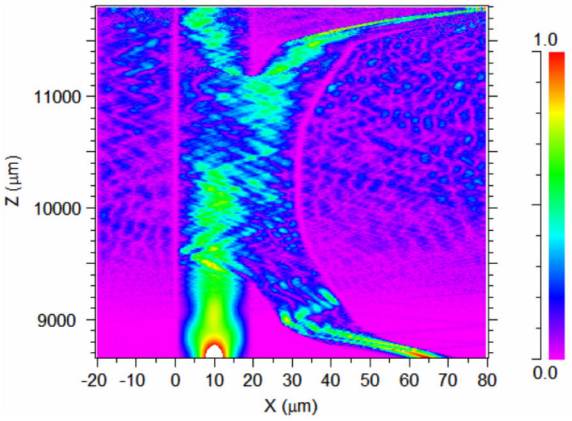

Fig. 9 *Simulation obtained before increasing the grid and changing the index profile*

The coefficient 'a' was multiplied by 2, 3, 5 and 8 achieving peak amplitude values of $2a \times 10^{-3}$, $3a \times 10^{-3}$, $5a \times 10^{-3}$ and $8a \times 10^{-3}$, respectively.

The magnitude of this variation results reasonably from the experimental conditions of micromachining that allows changes of the refractive index in the proposed range [17].

As support for this, there are retrieval methods algorithms for testing refractive index changes in waveguides written in transparent materials that confirm this order of magnitude [23].

Figs. 7 and 8 show that the scattering was progressively reduced inasmuch that the multiplier of the refractive index profile increases (by comparison with Fig. 9). In this sense, it can be observed that almost no energy was spread outside of the waveguides. However, despite the good confinement, the coupled energy to the ring is lower than expected so there is an increase of the energy guided by the bus, for each value of refractive index change analysed.

5 Conclusions

In this paper, the results of losses and guiding performance for large rings designed by using standard simulations tools allowed us to recognise two main challenges to be solved.

The first one was to determine the optimal number of sides needed to avoid scattering losses in agreement with conditions of coherent coupling theory. The second one was the splice angle. This deduction allows us explaining that software representation of a circular geometry as many sides polygon use a default splice angle larger than the most suitable. Finally, we found that in this closed polygon the best number of sides was 250.

On the other hand, the BMP method allowed simulations with success considering the strategy of two zones division, over-passing the necessity of one-way propagation. As a model of index profile, the combination of Gaussian curves has shown good performance in the simulation projects. Little changes in the peak amplitude of these curves could minimise scattering losses. We thought this is physically reasonable because this variation occurs in a small zone which is centred in the red area of the waveguides.

Thanks to this innovative design procedure, we can implement middle range ring resonator based on criteria taken from simulations, to define splice angles, shape and length for polygon segments and minimise the bending losses.

6 Acknowledgments

This work was partially supported by the Agencia Nacional de Promoción Científica y Tecnológica (Argentina) under the project PICT-2016-4086, PICT-2017-0017, and by Universidad Nacional de Quilmes (Argentina) under project PPROF-901-2018. RRP, DP and GAT are with CONICET, FV is with CICBA-CSBS-FI-UNLP and PP is with UNLP.

7 References

[1] Titterton, D., Weston, J.L., Weston, J.: '*Strapdown inertial navigation technology*', vol. **17**, (IET, UK, 2004)

[2] Vannahme, C., Suche, H., Reza, S., *et al.*: 'Integrated optical ti: Linbo3 ring resonator for rotation rate sensing'. Proc. 13th ECIO, Copenhagen, Denmark, 2007

[3] Guarino, A.: '*Electro-optic microring resonators in inorganic crystals for photonic applications*'. PhD thesis, ETH Zurich, 2007

[4] El-Fiky, E., Osman, M., Sowailem, M., *et al.*: '200 gb/s transmission using a dual-polarization o-band silicon photonic intensity modulator for stokes vector direct detection applications', *Opt. Express*, 2017, **25**, (24), pp. 30336–30348

[5] Li, G., Winick, K.A., Youmans, B.R., *et al.*: 'Design, fabrication and characterization of an integrated optic passive resonator for optical gyroscopes'. Proc. of the 60th Annual Meeting of The Institute of Navigation, Long Beach, CA, USA, 2001, pp. 211–216

[6] Ciminelli, C., Dell'Olio, F., Campanella, C.E., *et al.*: 'Photonic technologies for angular velocity sensing', *Adv. Opt. Photonics.*, 2010, **2**, (3), pp. 370–404

[7] Tejerina, M.R., Torchia, G.A.: 'Alternative configuration for an optical ring resonator angular rate sensor by using a standard laser diode', *Appl. Opt.*, 2011, **50**, (20), pp. 3449–3454

[8] Johnson, L.M., Leonberger, F.J.: 'Low-loss linbo3 waveguide bends with coherent coupling', *Opt. Lett.*, 1983, **8**, (2), p. 111

[9] Kim, S.-H., Kim, D., Jeon, S.-J., *et al.*: 'Analysis of regular polygonal ring resonator based on multi-mode waveguide', in *'Integrated optics: devices, materials, and technologies XXIII'*, vol. **10921**, (International Society for Optics and Photonics, USA, 2019), p. 109211L

[10] Taylor, H.F.: 'Power loss at directional change in dielectric waveguides', *Appl. Opt.*, 1974, **13**, (3), p. 642

[11] Suzuki, K., Takiguchi, K., Hotate, K.: 'Monolithically integrated resonator microoptic gyro on silica planar lightwave circuit', *J. Lightwave Technol.*, 2000, **18**, (1), pp. 66–72

[12] Ciminelli, C., Dell'Olio, F., Campanella, C.E., *et al.*: 'Numerical and experimental investigation of an optical high-q spiral resonator gyroscope'. In 2012 14th Int. Conf. on Transparent Optical Networks (ICTON), Coventry, UK, 2012, pp. 1–4.

[13] Rabus, D.G.: '*Integrated ring resonators*' (Springer, Germany, 2007)

[14] Levy, S., Klebanov, M., Zadok, A.: 'High-q ring resonators directly written in as_2s_3 chalcogenide glass films', *Photonics Res.*, 2015, **3**, (3), p. 63

[15] Wei, H., Krishnaswamy, S.: 'Polymer micro-ring resonator integrated with a fiber ring laser for ultrasound detection', *Opt. Lett.*, 2017, **42**, (13), p. 2655

[16] Presti, D., Videla, F.A., Torchia, G.A.: 'Optical fiber ring resonator as a high-resolution spectrometer. characterization and applications with single line diode lasers', *Opt. Eng.*, 2018, **57**, (5), p. 057108

[17] Tejerina, M.R., Jaque, D., Torchia, G.A.: 'A 2d μ -Raman analysis of low repetition rate femto-waveguides in lithium niobate by using a finite element model', *Opt. Mater.*, 2014, **36**, (5), pp. 936–940

[18] Chen, F., Vázquez de Aldana, J.R.: 'Optical waveguides in crystalline dielectric materials produced by femtosecond-laser micromachining', *Laser Photonics Rev.*, 2014, **8**, (2), pp. 251–275

[19] Presti, D.A., Guarepi, V., Videla, F., *et al.*: 'Modeling of the refractive index profile of a femtosecond written waveguide in linbo3'. in *'Photonic fiber and crystal devices: advances in materials and innovations in device applications XIII'*, vol. **11123**, (International Society for Optics and Photonics, USA, 2019), p. 111230Q

[20] Tejerina, M., Torchia, G.A.: 'Matfesa: strain and refractive index field estimation after femtosecond laser interaction with transparent material', *Appl. Phys. A*, 2013, **110**, (3), pp. 591–594

[21] Su, J.-J., Wang, W.-S.: 'Novel coherently coupled multisectional bending optical waveguide', *IEEE Photonics Technol. Lett.*, 2002, **14**, (8), pp. 1112–1114

[22] Peyton, R., Guarepi, V., Videla, F., *et al.*: 'Key kinematic parameters in a low-loss power splitter written by femtosecond laser micromachining', *J. Micromech. Microeng.*, 2018, **28**, (5), p. 055011

[23] Biasetti, D.A., Tejerina, M.R., Torchia, G.A.: 'Low contrast buried waveguides index profile reconstruction method considering the evanescent field', *J. Opt.*, 2015, **17**, (8), p. 085801